Incorporation of Past CPI Data into Knowledge-Aided STAP Processing

Douglas Page, Steven Scarborough, Gregory Owirka, Steven Crooks

***Abstract*—A technique for incorporating past coherent processing interval (CPI) radar data into knowledge-aided space-time adaptive processing (STAP) is described. The technique employs an earth-based clutter reflectivity map to provide improved knowledge of clutter statistics in nonhomogeneous terrain environments. The map is utilized to calculate predicted, current CPI covariance matrices as a function of range. Using the KASSPER Data Set, predicted clutter statistics are compared to measured statistics to verify the accuracy of the approach. Robust STAP weight vectors are calculated by combining the predicted covariance estimates with standard single CPI estimates using a published knowledge-aided pre-whitening algorithm. Target detection performance is also evaluated on the KASSPER Data Set and compared to that of standard STAP processing. Several performance metrics are calculated, including signal-to-interference plus noise (SINR) loss, target detections and false alarms, receiver operating characteristic (ROC) curves, and tracking performance. The results show a significant benefit to using knowledge-aided processing based on a past CPI reflectivity map.**

I. Introduction

THE lack of training data in nonhomogeneous clutter environments can cause severe degradation in the performance of space-time adaptive processing (STAP) algorithms (see [1,2] and references contained therein). Under the Defense Advanced Research Projects Agency (DARPA) Knowledge Aided Sensor Signal Processing and Expert Reasoning (KASSPER) program, ALPHATECH has been studying techniques to improve STAP performance in such environments.

Surveillance radars typically perform STAP processing on a limited number of pulses of data which is referred to as a coherent processing interval (CPI). Covariance estimation for STAP is usually performed by averaging over range-gates on a single CPI. Due to varying terrain conditions, however, this may result in poor estimates due to an inadequate amount of training data matching the range-gate under test. Two possible consequences of this are undernulling or overnulling of clutter. Undernulling may occur if the test range-gate contains strong clutter due to, say, steeply sloped terrain, while the training window surrounding the test cell contains less severe clutter. This may lead to an excessive number of false alarms or, if the threshold is increased to reduce false alarms, loss of target detections. Overnulling of clutter may occur when the training window contains steeply sloped terrain or windblown clutter that is not present in the target range cell. Overnulling leads to the loss of target detections.

The motivation for the study described here is the fact that in surveillance radar scenarios a given area on the ground may contribute to clutter returns over *multiple* CPIs. The data-cubes from these CPIs contain potential training data for estimating covariance matrices which, if exploited properly, could reduce the degradation caused by range-varying terrain. Additionally, a priori information about the surveillance area in a given mission can be obtained through databases. Digital terrain elevation data (DTED) allows precise registration of ground scatterer locations in radar-centered coordinates on different CPIs. In combination with land use/land cover information, DTED can also be used to calculate clutter statistics based on pre-stored clutter models. These models, however, may have errors due to inaccurate clutter models, out-of-date databases, etc. Combining such predictions with local clutter estimates derived from past CPI data may provide the best solution for reducing the

The authors are with ALPHATECH, Inc., 6 New England Executive Park, Burlington, MA 01803

amount of over/under-nulling and maximizing knowledge-aided STAP performance.

Due to the fact that the platform geometry is changing from CPI to CPI, simply averaging outer products of complex returns from additional CPI data-cubes to augment standard covariance estimation is not effective. The changing platform geometry means that the range-gate footprints on the ground are also changing with CPI. In addition to this, the Doppler frequency of a given point on the ground will be changing with CPI. Thus, in order to exploit the past CPI data, a STAP algorithm must be able to 1) extract information on clutter statistics as a function of ground location and 2) correct for the differences in the range and Doppler locations of clutter scatterers on different CPIs.

Even if the range/Doppler variation of the ground scatterers were perfectly known, there may also be differences in clutter returns on different CPIs due to changing antenna element gains on the scatterers and aspect-dependent reflectivity. Due to such effects, there will inevitably be errors in the knowledge of clutter statistics gained from past CPI data-cubes. The algorithm that is developed needs to be robust against these errors, and may need to incorporate an appropriate combination of covariance estimates that are derived on the current CPI using a conventional range-averaging procedure with estimates based on past CPI data.

We describe in section II the approach that was developed for accomplishing the objectives described above. In section III, we show the results of processing on the KASSPER Data Set 2 [3], which simulates a radar clutter environment under "real-world" conditions. The results obtained indicate that significant improvements in STAP performance may indeed be achieved by utilizing past CPI data.

II. Description of the Algorithm for Incorporating Past CPI Data

As mentioned in the Introduction, in order to exploit past CPI data in STAP processing one must correct for CPI-to-CPI differences in range and Doppler frequency of the clutter scatterers on the ground. The approach taken to accomplish this was to form an earth-based clutter reflectivity map. This map contains information on clutter reflectivity (clutter power per unit area), averaged over a spatial area on the ground and over multiple CPIs. The registration of data from different CPIs was produced by converting the locations of the clutter scatterers in each CPI from radar-centered to earth-centered coordinates. To predict clutter statistics on the current CPI, the reflectivities of the scatterers in each range-gate were retrieved by again converting to earth-centered coordinates and accessing the appropriate cells of the reflectivity map. In order to produce robust STAP performance in the presence of errors, a recently published knowledge-aided pre-whitening technique was employed [4].

In this section we describe the three main aspects of the algorithm as follows. We first describe in sub-section *A* the steps required for the formation of the clutter reflectivity map. In sub-section *B* we describe how the map was used to derive clutter statistics on the current CPI. The statistics were verified by comparing measured and predicted range-Doppler spectra of portions of the KASSPER Data Set. Finally, in sub-section *C* we describe the knowledge-aided pre-whitening technique that was used to combine the covariance estimates derived from the clutter reflectivity map with the training data from the current CPI. This combination results in a STAP weight vector that is robust to errors in the knowledge of the clutter statistics derived from the past CPI data.

A. Formation of a clutter reflectivity map

The first aspect of the algorithm for incorporating past CPI data was to form a clutter reflectivity map based on multiple CPI data-cubes. This process is illustrated in Figure 1. There are four basic steps involved in forming this map:

1. Define clutter scatterers in each processed range-gate of each past CPI data-cube
2. Calculate the scatterer locations in an earth-based coordinate system (i.e. *geo-register* the scatterers)
3. Estimate the amplitude of each of the scatterers in the received radar returns
4. Normalize the scatterer amplitudes by their area on the ground, and form an average earth-based clutter reflectivity map

These steps are described individually in more

detail below.

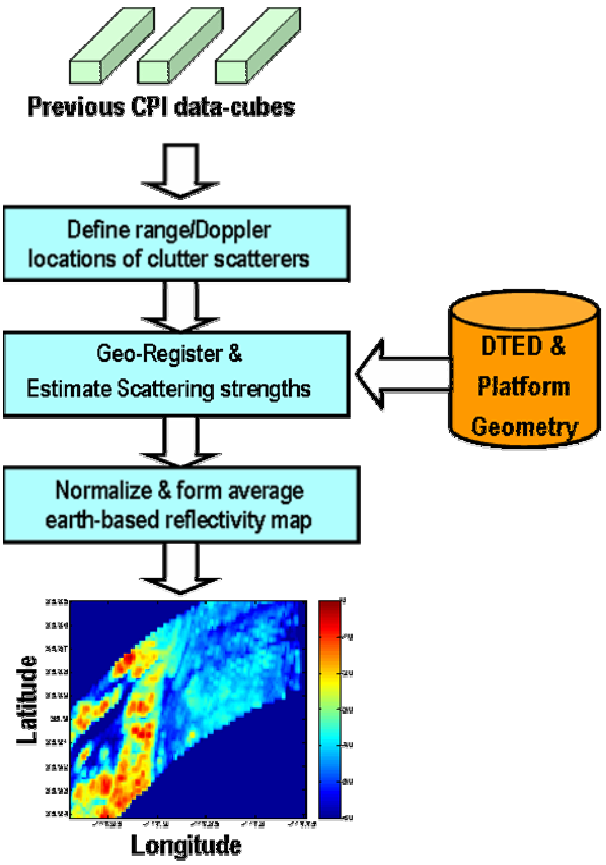

Figure 1 Illustration of procedure for forming an earth-based clutter reflectivity map

A.1 Definition of clutter scatterers

The first step in the algorithm was to define a discrete set of ground scatterers in each range-gate of each past CPI data-cube. The contributions of different scatterers on the ground to a radar return in a given range-gate of a given CPI are distinguished by their spatial response across the receive antenna array elements and their temporal response across the pulses of the CPI. To obtain accurate representation of the clutter statistics, the discrete scatterers that are assumed in each range-gate should be spaced so that the changes in spatial angle and Doppler frequency do not exceed the corresponding spatial and Doppler radar resolution respectively. A finer spacing is possible, provided that the algorithm used to estimate the scattering strengths can accurately determine the variation of scattering strength with ground location (essentially, such an algorithm would be performing super-resolution estimation).

The spatial resolution of a surveillance radar is limited by the antenna size, which determines the antenna beamwidth. The Doppler resolution is given by the inverse of the time extent of the CPI (which is also the width of a Doppler filter if unweighted Fourier transform processing is employed). Table I lists relevant parameters of the KASSPER Data Set that was processed.

TABLE I
RELEVANT PARAMETERS OF THE KASSPER DATA SET [3]

Quantity	Value
Radar frequency	10 GHz
Radar bandwidth	10 MHz
Peak power	10 kW
System losses	7 dB
Antenna size	1.43 m (horizontal) by .285 m (vertical)
Transmit antenna pattern	Spoiled to 10 degrees beamwidth
Receive antenna configuration	12 non-overlapping subarrays, spaced by 4 wavelengths per subarray
Number of pulses per CPI	38
Number of CPIs per dwell	3 with PRFs of 2081, 1800, and 1518 Hz
Time separation of dwells	10 seconds
Number of dwells in scenario	30
Platform motion	150 m/s, heading west
Crab angle	3 degrees
Standoff range to targets	Approximately 45 km
Target clusters	3 clusters, 60 vehicles each
Background traffic	1000 vehicles
Target motion	Move along roads, speed 2-25 m/s depending on road type, decelerate when approaching intersections
Earth model	Spherical, radius 6378388 m, modulated by DTED

The antenna elements of the KASSPER Data Set were formed using 12 non-overlapped subarrays spaced by 4 wavelengths per subarray. The subarrays were pre-steered to a particular direction on each CPI. The azimuth and elevation angle of this pre-steering direction were supplied along with

the data-cube for each CPI. Each CPI contains 38 pulses, and a dwell consisting of three consecutive CPIs at different pulse repetition frequencies (PRFs) occurs every 10 seconds. During this time interval, the platform moves 1.5 km, which is significant relative to the 40 km standoff range to the targets (small changes in aspect can produce large changes in covariance matrices).

The radar parameters shown in Table I lead to a Doppler filter width on the ground that is significantly smaller than the antenna beamwidth. At broadside, the azimuth width of a Doppler filter is given by

$$\Delta\theta \approx \frac{\lambda}{2 \cdot V_a \cdot M \cdot T_r} \approx \frac{.03}{2 \cdot 150 \cdot 38 \cdot .0005} = 5.3 \cdot 10^{-3} \text{ radians} = .3 \text{ degrees}$$

The antenna azimuth beamwidth, on the other hand is given approximately by

$$\lambda / D = .03 / 1.43 = .021 \text{ radians} = 1.2 \text{ degrees}$$

Thus the Doppler filter spacing is about ¼ of the antenna beamwidth (as one moves off broadside, the Doppler filter width and antenna beamwidth both increase by a factor of $1/\cos\theta_{steer}$). Consequently, defining the scatterers in each range-gate by their Doppler frequency, and spacing them apart by no more than one Doppler filter should result in satisfying both the spatial and temporal resolution requirements.

Given the considerations discussed above, the scatterers in each range-gate of each past CPI data-cube were defined by specifying 1) their range from the radar platform and 2) their Doppler frequency. The range of each scatterer in a given range-gate was defined to be the slant range at the center of the range-gate. The bandwidth of the system shown in Table I leads to a range resolution of 15 m, which is much smaller than the size of the antenna beams or Doppler filters on the ground. Thus, one scatterer per range cell should suffice to give accurate clutter statistics.

The Doppler frequencies of the scatterers were defined to span multiple Doppler ambiguities about the Doppler frequency at the radar look direction. For the KASSPER Data Set, three Doppler ambiguities were modeled in order to make sure that all mainlobe and near-sidelobe clutter was represented. The Doppler spacing between adjacent scatterers was taken to be one Doppler filter. Figure 2 below shows the Doppler frequencies and azimuth angles of the scatterers that were defined in one range-gate of a past CPI data-cube. These lie along the so-called Doppler-angle "clutter ridge" (actually, the azimuth angles of the scatterers were calculated *after* the geo-registration step discussed below).

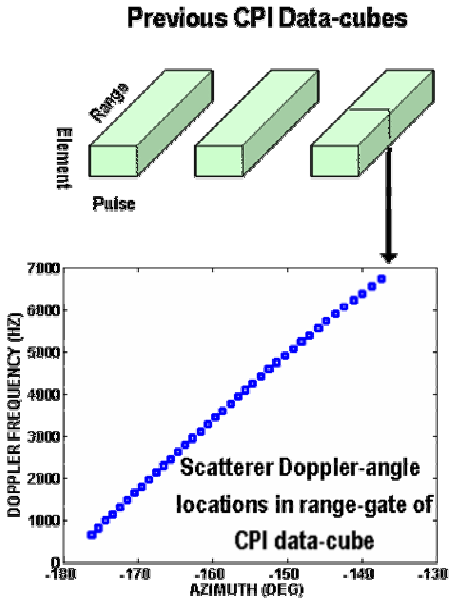

Figure 2 Doppler-angle locations of clutter scatterers in one range-gate of a past CPI data-cube

A.2 Geo-registration of scatterer locations

Once the slant range and Doppler frequencies of the possible ground scatterers were defined, the next step was to compute earth-based coordinates for the scatterers. The ground location of a scatterer is determined by the intersection of three surfaces:

a) a range sphere centered on the platform location, having a radius equal to the slant range R_s of the scatterer

b) a cone about the platform velocity vector, corresponding to the Doppler frequency of the scatterer. Neglecting internal clutter motion, the cosine of the cone angle relative to the platform velocity vector is given by

$$\cos\theta_c = \frac{\lambda f_{dop}}{2V_p}, \quad (1)$$

where λ is the radar wavelength, f_{dop} the scatterer Doppler frequency, and V_p the radar platform speed.

c) the earth's surface. This is defined by digital terrain elevation data (DTED). A level 1 database indexed by latitude and longitude having a posting of 90 m was employed (note from Table I that in the KASSPER Data Set these height variations are assumed to occur on a reference spherical earth).

The height of the earth's surface at a scatterer location depends on its latitude and longitude, and these are unknown. For the moment, assume that the height h of the terrain above the reference spherical earth model of radius R_e is known. Let the unknown position of the scatterer in earth-centered coordinates be denoted by $\vec{r}_{sc}$. The platform position vector is known and is denoted by $\vec{r}_p$. The scatterer position is then determined by the following three equations:

$$\begin{aligned} &|\vec{r}_{sc} - \vec{r}_p|^2 = R_s^{\,2} && \text{(range sphere)} \\ &(\vec{r}_{sc} - \vec{r}_p) \bullet \vec{V}_p = R_s \cdot V_p \cdot \cos\theta_c && \text{(Doppler cone)} \\ &|\vec{r}_{sc}|^2 = (R_e + h)^2 && \text{(earth sphere)} \end{aligned} \quad (2)$$

The above equations constitute a set of three equations and three unknowns, which are the three components of the scatterer position vector $\vec{r}_{sc}$. The method that was used to solve these equations to determine $\vec{r}_{sc}$ is detailed in appendix A.

We accounted for the fact that the height h is unknown by employing the following iterative procedure:

1. Intitialize the scatterer height h above the earth using the DTED derived height for a reference lat/lon in the surveillance volume
2. Calculate the intersection of the range sphere, Doppler cone, and earth sphere in earth-centered coordinates by solving Eqs. (2) for the three components of $\vec{r}_{sc}$
3. Convert $\vec{r}_{sc}$ to latitude and longitude using spherical earth geometry
4. Fetch the value of the DTED-derived height at the latitude and longitude determined in 3.
5. Repeat steps 2-4 until the difference in height is small.

The above procedure results in earth-based geodetic coordinates for each of the clutter scatterers defined in *A.1* for each past CPI data-cube.

A.3 Estimation of scatterer strengths

Once the scatterer locations on the ground were determined, their contributions to the received radar amplitudes were estimated. This first required defining the steering vector to each scatterer. A steering vector describes the space-time response of a unit amplitude scatterer. Mathematically, it is a direct product of the spatial response across the antenna elements and the temporal response across the pulses in the CPI. Letting N denote the number of antenna elements, and M the number of pulses in a CPI, the steering vector to each of the scatterers will be given by a NM by 1 column vector. The elements of the vector are a function of the look direction to the scatterer and its Doppler frequency. The effects of atmospheric refraction on the look direction were taken into account using an effective earth model. The precise form of the elements of the steering vectors that was employed is given in Appendix B.

For the present discussion, let the steering vector to the scatterer i in a given range-gate of a given data-cube be denoted by $\vec{s}_i$. Also let $\vec{x}$ be the measured data vector in the range-gate. We desire an approximation of $\vec{x}$ in the form

$$\vec{x} = \sum_i \alpha_i \cdot \vec{s}_i \quad (3)$$

The complex return strengths α_i were selected in order to minimize the squared error

$$\varepsilon = |\vec{x} - \sum_i \alpha_i \cdot \vec{s}_i|^2 \quad (4)$$

The solution of this problem can be shown to be

$$\alpha_i = \sum_j [S^{-1}]_{ij} \cdot \vec{s}_j{}^H \vec{x}, \quad (5)$$

where the matrix S is defined by the elements

$$[S]_{ij} = \vec{s}_i{}^H \vec{s}_j \tag{6}$$

In general, the matrix S will not be diagonal, due to the fact that the steering vectors will not be orthogonal. This is true even if the scatterer spacing is selected to be one Doppler filter, due to the fact that multiple Doppler ambiguities are modeled.

The complex numbers α_i represent the return strengths of the scatterers in a given range-gate of a given data-cube. Each of the scatterers represents clutter in one range-Doppler cell, which in turn corresponds to a particular area on the ground. The procedure described here is repeated for all the processed range-gates in each of the CPI data-cubes used to form the reflectivity map.

A.4 Normalization and formation of reflectivity map

Since the complex clutter estimates obtained in *A.3* were derived from measured data, they implicitly include all the effects of parameters appearing in the radar range equation (i.e. antenna patterns, clutter radar cross section, etc.). Because the areas of range-Doppler resolution cells on the ground will be changing from CPI to CPI, it is important to build the clutter reflectivity map using reflectivities rather than complex clutter strengths (the cell areas are different on each CPI due to the different PRFs, as well as the changing geometry as the platform moves). The clutter reflectivity is defined here as the clutter power $|\alpha|^2$ of a given scatterer divided by the area on the ground represented by that scatterer.

The cell area of each scatterer on the ground was determined using the earth-centered Cartesian coordinates ($\vec{r}_{sc}$) of the scatterers that are adjacent in range and Doppler. Vectors connecting these adjacent scatterers define the size of the cell represented by the scatterer under consideration. Define $\Delta\vec{r}_{rng}{}^{(i)}$ as the vector on the ground spanning the range dimension of scatterer *i,* and $\Delta\vec{r}_{dop}{}^{(i)}$ as the vector spanning the Doppler dimension. The area of the corresponding ground cell is then given by

$$A_i = |\Delta\vec{r}_{rng}{}^{(i)} \times \Delta\vec{r}_{dop}{}^{(i)}| \tag{7}$$

The reflectivity map was built by averaging the clutter reflectivity values of all the scatterers over multiple CPIs and range-gates lying within each of the latitude/longitude cells defining the map:

$$\rho(ilat, ilon) = \frac{1}{N_{sc}} \sum_{\substack{\text{scatterers } i \text{ lying} \\ \text{in cell } ilat, ilon}} \frac{|\alpha_i|^2}{A_i}, \tag{8}$$

Here, N_{sc} is the number of scatterers lying within the cell indexed by *ilat,ilon*. The reflectivity of a given cell in the map is thus an average over scatterers in all processed range-gates and CPIs lying within the cell.

The resolution of the map was selected as 200 m, reflecting the typical size of a Doppler resolution cell (which is 240 m for terrain located off broadside at 45 km range). While this is significantly larger than the 15 m range resolution, it allows a large number of training samples to be averaged within each cell of the map. This in turn provides a smoothing of the map. In addition, the algorithm used to estimate of scatterer strengths described above has a resolution that is limited by the Doppler cell width. Thus, defining a cell size much smaller than the Doppler filter width would not produce a correspondingly accurate representation of the behavior of the clutter reflectivity from cell to cell.

Figure 3 shows a clutter reflectivity map that was calculated based on 10 CPIs. The boundaries of the map correspond to the range boundaries of the CPIs that were processed. The reflectivity map is seen to predict regions of very strong clutter, which are produced by steeply sloped terrain. In addition there are areas where the reflectivity is much weaker which includes regions that are shadowed from the radar (i.e. not visible). The knowledge gained from the reflectivity map allows these areas to be identified. The STAP processor can incorporate this knowledge into the adaptive weight vector and reduce the magnitude of over/undernulling that occurs with standard range-averaged covariance estimation.

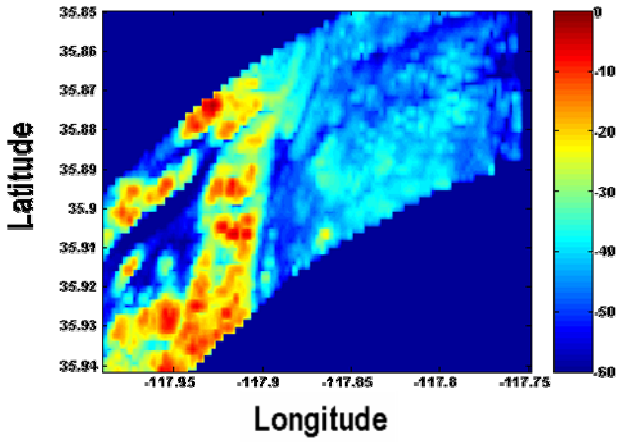

Figure 3 Clutter reflectivity map formed from multiple CPIs of the KASSPER Data Set

B. Prediction of current CPI clutter statistics

Once a reflectivity map based on past CPIs is formed, it must then be employed to calculate clutter statistics for the current CPI. The procedure used here was to define a grid of scatterers in each range-gate of the data-cube, as described in sub-section *A.1*, spanning three Doppler ambiguities about the look direction (the only difference was that the spacing of the scatterers in Doppler was taken to be half a Doppler filter rather than one filter). Registration to geodetic coordinates was also performed as described in sub-section *A.2*. The steering vectors $\vec{s}_i$ and cell areas A_i of each scatterer were then calculated as specified in sub-section *A.3*.

The reflectivity ρ_i of scatterer i of the current CPI data-cube was determined by using its calculated latitude and longitude and indexing into the clutter reflectivity map. To obtain the estimated power p_i of scatterer i, the reflectivity was multiplied by the cell area A_i of the scatterer. A correction for the overall antenna subarray pattern was also applied to account for scatterers that may have been in the mainlobe on previous CPIs but have moved into the antenna sidelobes on the current CPI. A covariance matrix for each range-gate was then calculated by summing the individual contributions of the scatterers in the range-gate:

$$R_{calc} = \sum_i p_i \cdot \vec{s}_i \vec{s}_i^{\,H} \qquad (9)$$

To test the accuracy of the algorithm, a plot of the mean power in each range-gate and Doppler filter was calculated. This was done by employing a single spatial weight vector corresponding to the radar look direction and a bank of temporal weight vectors corresponding to a temporal FFT across the CPI. Chebychev weighting (60 dB sidelobes) was applied across the pulses prior to applying the weight vectors in order to reduce the effects of Doppler sidelobes.

Figure 4 shows measured range/Doppler spectra of four different CPIs that were used to form the reflectivity map shown in Figure 3. The clutter in these plots is somewhat confined in Doppler (vertical dimension). This is due to the Doppler extent of the area covered by the antenna beamwidth. The Doppler extent of the plots is equal to the PRF of the corresponding CPI. The Doppler interval was oversampled so that the number of Doppler frequencies at which the spectrum was evaluated was equal to two times the number of pulses in the CPI. Note the strong range variation of the clutter (the range extent of the plots is 2.7 km). This is due to the occurrence of varying terrain slopes and shadowing.

Note in addition that the Doppler location of the clutter is different in each CPI. Also, the shape of the clutter spectra is slightly different for each CPI. As discussed earlier, this is due to the fact that the platform geometry is different on each CPI. Additionally, the PRFs are different on some of the CPIs, which causes changes in the Doppler index location of the clutter, as well as the magnitude of the clutter returns through the size of the Doppler filters on the ground. The purpose of performing geo-registration of the scatterers and forming the earth-based clutter map is to correct for all these differences.

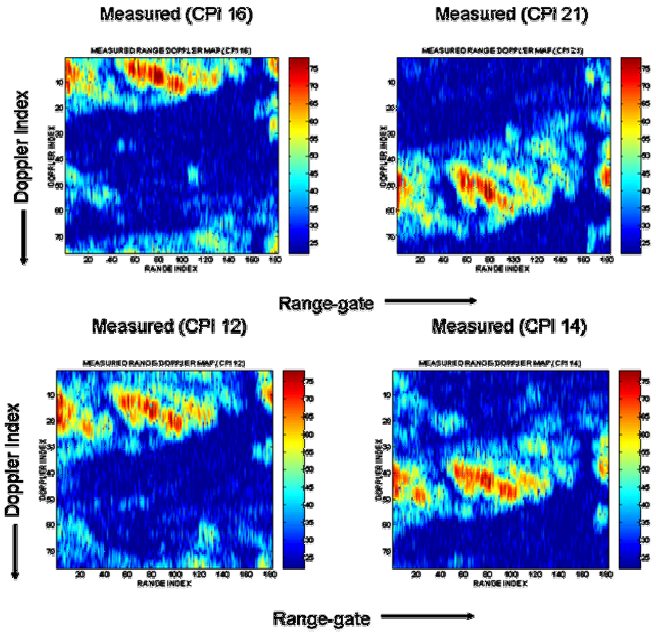

Figure 4 Measured range-Doppler spectra for portions of four different CPIs of the KASSPER Data Set

Figure 5 compares the measured range/Doppler spectrum for CPI 22 with the mean spectrum corresponding to the covariance matrices calculated using the reflectivity map shown in Figure 3. The main features are modeled as could be expected from a 200 meter resolution. The clutter location in Doppler and its variation with range is correctly predicted, showing that the registration procedure was effective. The green colored returns in the middle of the plots are due to near sidelobe clutter and are also correctly predicted.

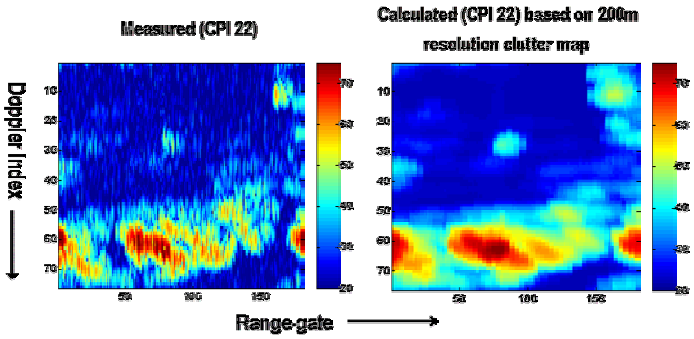

Figure 5 Comparison of measured range-Doppler spectrum for CPI 22 (left) with prediction of clutter reflectivity map (right)

For comparison, Figure 6 shows the mean Doppler spectrum of a range-averaged covariance (a single covariance matrix formed by averaging over 181 range-gates was used to obtain this figure). Note that forming a range-averaged covariance smears out the variations over the extent of the training window. Upon comparison of Figs. 5 and 6 it is seen that the calculated covariance certainly models the features more accurately than a single range-averaged covariance matrix. The latter is representative of the prediction produced by the standard STAP training procedure.

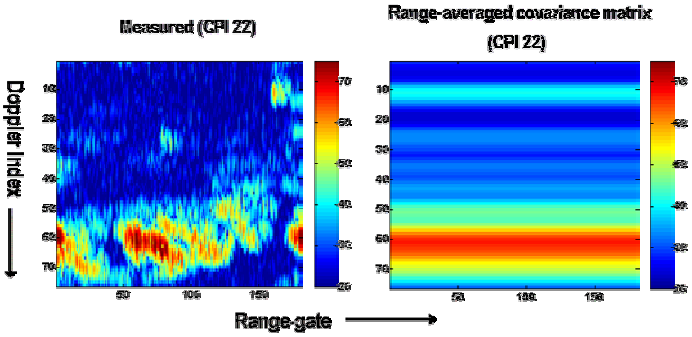

Figure 6 Comparison of measured range-Doppler spectrum for CPI 22 (left) with prediction based on a single range-averaged covariance matrix (right)

C. Calculation of STAP weight vector

Due to such effects as unknown internal clutter motion, antenna element pattern variations, and aspect-dependent reflectivity, there will be errors in the clutter covariance matrices calculated from the reflectivity map. Conventional covariance estimation based on current CPI data includes these effects to some extent. Internal clutter motion and antenna pattern mismatch are implicitly included in the measured range-averaged covariance matrices derived from the current CPI data-cube. However, the clutter reflectivity (and perhaps internal clutter motion as well) will be range varying, which leads to degradation of conventional STAP performance. What is needed is an algorithm that "fuses" the estimates provided by the clutter reflectivity map with those calculated directly from the current CPI data. The desired algorithm would utilize the reflectivity map to reduce the errors caused by range-varying clutter statistics in the current CPI data-cube, yet be robust to effects such as antenna pattern mismatch and internal clutter motion.

To this end, we applied an algorithm that was presented by Bergin [4] at the 2003 Adaptive Array Sensor Processing (ASAP) conference. This algorithm fuses a calculated covariance matrix with an estimated covariance to calculate a robust STAP weight vector. The STAP weight vector is given by

$$\vec{w} = \kappa(R_{curr} + \beta_l \cdot I + \beta_d \cdot R_{calc})^{-1}\vec{s} \qquad (10)$$

Here R_{curr} is the conventional covariance estimate derived from the current CPI data-cube, R_{calc} is a calculated covariance matrix, $\vec{s}$ is the target steering vector, β_l is the conventional diagonal loading scale factor, and β_d is a "colored loading" scale factor. The factor κ is an overall scalar multiplier. It was also shown in [4] that the above STAP weight vector could also be implemented using a pre-whitening approach. In this approach, the data vector and the diagonally loaded range-averaged covariance estimate are pre-whitened using the calculated covariance matrix.

We applied the above algorithm for calculating the STAP weight vector to the KASSPER Data Set in a post-Doppler framework. In particular, an extended-factored [5] (also known as "adjacent bin" or "multi-bin" post-Doppler) algorithm was implemented. This algorithm calculates a separate STAP weight vector in each Doppler filter. The spatial degrees of freedom (DOFs) consisted of all of the 12 antenna subarrays, while the temporal DOFs consisted of 5 Doppler filters surrounding the filter under test.

A post-Doppler approach has certain advantages over full DOF processing:

1) Due to the reduced number of DOFs (60 vs. 456 for the KASSPER Data Set), the size of the training range window can be reduced, thus providing more accurate local estimates of the clutter statistics. A training window equal to three times the number of DOFs was employed (180 range-gates, corresponding to a 2.7 km range extent for the KASSPER Data Set).

2) A separate STAP weight vector is used in each Doppler filter, allowing tailoring the adaptive filter to the clutter present in each Doppler filter. This is advantageous when the clutter is strongly varying with Doppler (as was seen in Figures 4 and 5)

3) The effects of strong discretes and targets can be separately suppressed from the covariance estimates in each Doppler filter.

To account for internal clutter motion, the calculated covariance matrices shown in Eq. (9) were modified before Doppler processing. Reference [6] shows that the effect of internal clutter motion on the covariance matrix is to taper the elements of that matrix. To model a two-sided exponential velocity distribution, a tapering function with a Lorentzian shape was applied to the elements of the covariance matrices calculated from the reflectivity map:

$$R_{nm,n'm'} \rightarrow R_{nm,n'm'} \cdot \frac{1}{1+\gamma\,|\,m-m'|^2} \qquad (11)$$

Here n, n' are spatial element indices, while m, m' are temporal pulse indices. The constant γ was selected to correspond to a .17 m/s standard deviation of the distribution of clutter internal velocity. This value was selected empirically based upon observations of the data correlation characteristics.

Once the covariance taper was applied to the calculated covariance matrices, Doppler pre-processing for the extended-factored algorithm was performed. This pre-processing defines, for each target Doppler frequency processed, a 60 by 456 transformation matrix *T*. The measured data vector and steering vectors were then transformed as

$$\vec{x} \rightarrow T\,\vec{x}, \quad \vec{s} \rightarrow T\,\vec{s}\,, \qquad (12)$$

while the measured and calculated covariance matrices were transformed as

$$R \rightarrow T\,R\,T^H \qquad (13)$$

(the "H" superscript means that the Hermitian conjugate is to be taken).

Equation (10) was used to calculate the STAP weight vector for each target Doppler frequency. The diagonal scale factor β_l was selected to produce diagonal loading at the noise floor. The colored loading scale factor β_d was selected so that the

mean power of the $\beta_d \cdot R_{calc}$ term matched that of the measured covariance R_{curr}. Finally, the overall scale factor κ was selected so that the absolute square after adaptive filtering produced the adaptive matched filter (AMF) test statistic [7]:

$$\kappa = \frac{1}{\sqrt{\vec{s}^{\,H}(R_{curr} + \beta_l \cdot I + \beta_d \cdot R_{calc})^{-1}\vec{s}}} \tag{14}$$

Adaptive filtering was then applied to the post-Doppler data vectors in each Doppler filter and in each range-gate using

$$y = |\vec{w}^{\,H}\vec{x}|^2 \tag{15}$$

The AMF statistic possesses an embedded constant false alarm rate (CFAR) property [7]. Therefore, the output amplitudes in Eq. (15) were thresholded directly to determine target detections and false alarms. The only additional CFAR processing was to perform a grouping of the threshold crossings near known target locations.

III. RESULTS OF PROCESSING ON THE KASSPER DATA SET

Before computing actual target detection performance, STAP performance was first evaluated by calculating signal to interference plus noise (SINR) loss. The SINR loss is defined by

$$L_{SINR} = \frac{|\vec{w}^{\,H}\vec{s}|^2}{\vec{w}^{\,H}R_{ideal}\vec{w} \cdot G_{noise}}, \tag{16}$$

Here, R_{ideal} is the ideal, exactly known clutter plus noise covariance and G_{noise} is the ideal, noise-limited SINR for a unit amplitude signal ($G_{noise} = NM = 456$ for the KASSPER Data Set). For CPI #22, the exact covariance matrices were provided in each range-gate, allowing computation of the SINR loss factor.

Figure 7 compares the SINR loss of a portion of this CPI for standard STAP processing versus knowledge-aided STAP processing using the algorithm described in section II. The loss is shown as a function of Doppler index (vertical) and range-gate (horizontal). The target Doppler interval was oversampled by a factor of two, so that the number of Doppler indices in the vertical dimension of the plots is equal to twice the number of pulses in the CPI (i.e. is equal to 76). The range extent is 2.7 km (equal to the extent of one training window). To obtain the results shown in Figure 7, data-cubes without targets were processed in order to isolate the benefits on clutter suppression produced by the past CPI reflectivity map.

Note from the plots that the SINR loss is degraded over a significant portion of the Doppler interval. This portion corresponds to the Doppler frequency of clutter over the antenna beamwidth. The range/Doppler extent of these plots is in fact the same as in Figure 5, and the region in which SINR loss is degraded can be compared to the areas of strong clutter return in Figure 5. Note however that with knowledge-aided processing the width of the "clutter notch" is significantly narrower in certain areas. This is due to improved knowledge of the local clutter statistics that is gained from the clutter reflectivity map. The 200 meter resolution of this map is much finer than the 2.7 km resolution of the standard training range window. It thus reduces the extent of over/under-nulling caused by the range varying clutter environment.

In addition to SINR loss, performance was evaluated by processing the data-cubes with targets in them and comparing threshold crossings to the known target range/Doppler locations. The effects of strong discretes and targets on the range-averaged covariance estimates were suppressed by performing separate range masking in each Doppler filter. To accomplish this, a two step procedure was employed:

1) Calculate the AMF statistic in each range/Doppler cell without any masking of the training data

2) Mask range/Doppler cells whose AMF statistic exceeded a certain threshold (15 dB) from the training data. Recompute the AMF statistic using the remaining training data and determine the resulting threshold crossings.

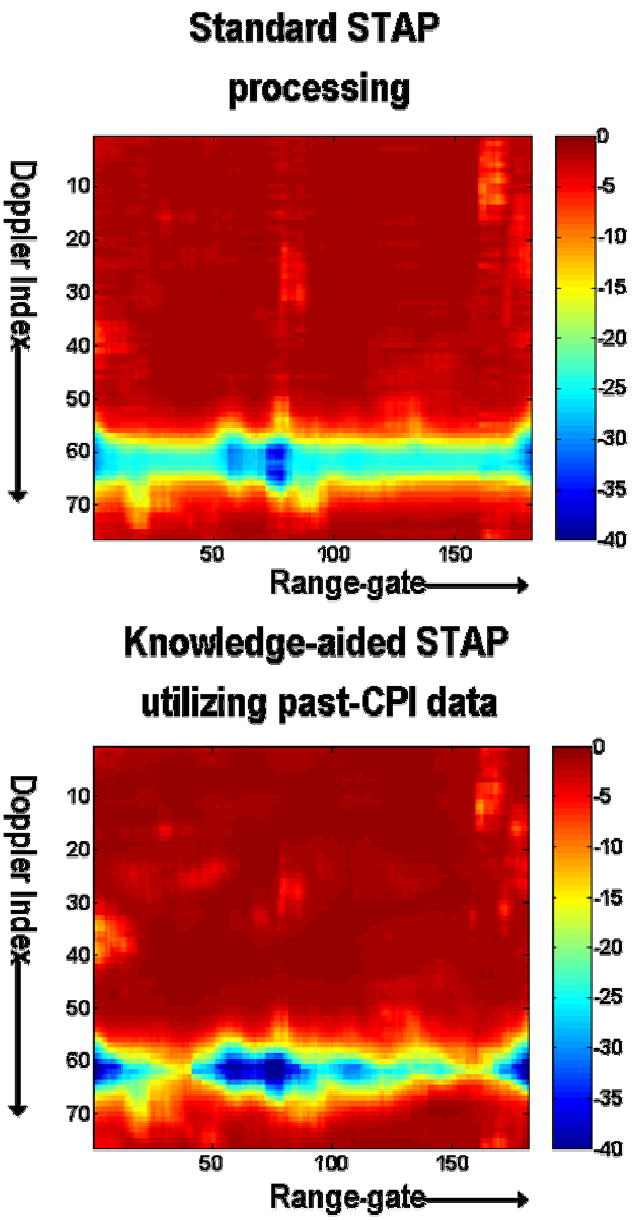

Figure 7 SINR Loss versus range (horizontal) and Doppler (vertical) for standard STAP processing (top plot) and knowledge-aided STAP processing (bottom plot)

Figure 8 compares the range/Doppler locations of threshold crossings in a portion of CPI #67 produced by standard STAP processing to those of knowledge-aided STAP (KASTAP) processing. The locations of known targets are shown as blue diamonds, while the threshold crossings are shown as yellow triangles. In each case there are false alarms present, which are due to returns from some very steeply sloped terrain. Note however that with KASTAP processing, there are fewer false alarms present and more detections at the locations of actual targets. This represents a significant benefit to using knowledge-aided processing that could translate into improved tracking of time critical targets.

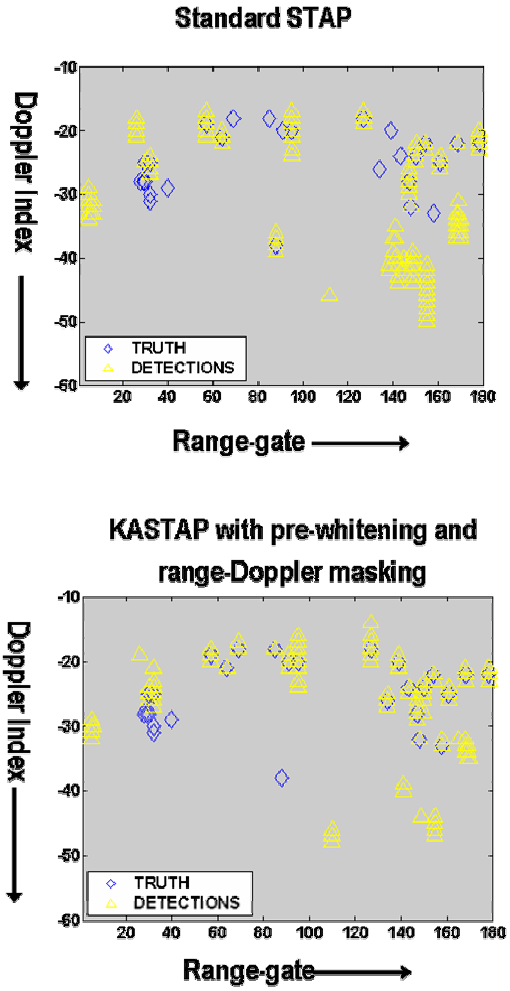

Figure 8 Range-Doppler locations of threshold crossings in a portion of CPI #67 for standard STAP processing (top plot) and knowledge-aided STAP processing (bottom plot)

In addition to individual examples of detections and false alarms, receiver operating characteristic (ROC) curves were generated. These were obtained by varying the AMF threshold and counting the number of target detections and false alarms for each threshold. Probability of detection was computed by calculating the fraction of targets within the range window processed that were detected. A significant number of closely spaced, non-moving targets were actually present in the scenes. Multiple targets lying within the same range/Doppler cell were counted as a single target.

Even after this was done, approximately 10% of the remaining targets were non-moving.

For each threshold setting, the false alarm density (number of alarms per square kilometer on the ground) was calculated. The range and azimuth extent processed corresponded to an area on the ground of 3 square kilometers per CPI. Composite performance was obtained over 23 CPIs. Only data-cubes having the 2081 Hz PRF were processed (if the two other CPIs with different PRFs were noncoherently combined on each dwell, improved performance could be expected). Figure 9 shows the results.

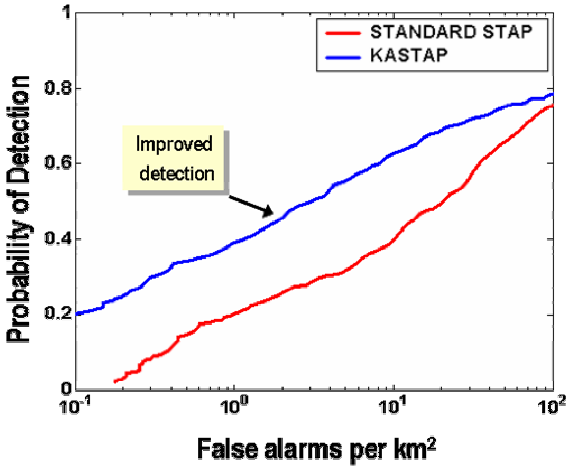

Figure 9 ROC curves over 23 CPIs for standard STAP processing (red) and knowledge-aided STAP processing (blue)

A consistent benefit in detection performance is seen from KASTAP processing. For example, at a detection probability of 60%, the false alarm density decreases from about 35 alarms per square kilometer for standard STAP processing to 8 per square kilometer for KASTAP processing, about a factor of 4 reduction. At a detection probability of 40%, the false alarm density decreases by almost a factor of 10, from roughly 10 alarms per square kilometer for standard STAP to about 1 per square kilometer for KASTAP. If the non-movers were removed from the data set, the detection probability values obtained would be expected to increase.

The effect of incorporating the clutter reflectivity map into knowledge-aided STAP processing on tracking performance was also evaluated using ALPHATECH's multiple hypothesis tracking (MHT) testbed. The KASSPER Data Set was again used; however only two of the targets from the data set were present in the scenario. Figure 10 shows target detections (yellow triangles) truth locations (brown diamonds), and track locations (red squares) for standard STAP vs. KASTAP processing for one of the dwells on the testbed display.

The yellow lines on the display represent the azimuth boundaries of the search region, and the green lines show the location of roads. The display is earth-referenced (i.e. North is up and East is to the right). For the dwell shown, range increases vertically downwards. Note that on this dwell standard STAP fails to detect the near range target, while each of the algorithms are tracking both of the targets. The standard STAP track for the near range target is being coasted and has been declared as off-road, due possibly to the turn in the road or to poor azimuth accuracy on the previous update.

Figure 11 shows tracking results over 23 dwells. Note that with KASTAP processing, the tracker was able to start the track sooner and there were fewer false alarms present. Together with the SINR loss and ROC performance differences that were observed, these results indicate that incorporating past CPI data into KASTAP processing may produce increased track life and fewer false tracks in critical military scenarios.

IV. Conclusion

We have described here a technique for incorporating past CPI data into knowledge-aided STAP processing. The algorithm corrects for differences between different CPI data-cubes, due to varying platform geometry and PRF, and forms an averaged earth-based clutter reflectivity map. The reflectivity map is then used to predict clutter statistics on the current CPI. Using the KASSPER Data Set, a sample reflectivity map was formed from multiple CPIs and shown to produce a range and Doppler variation that was in agreement with the measured clutter spectrum on a subsequent CPI.

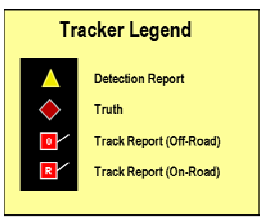

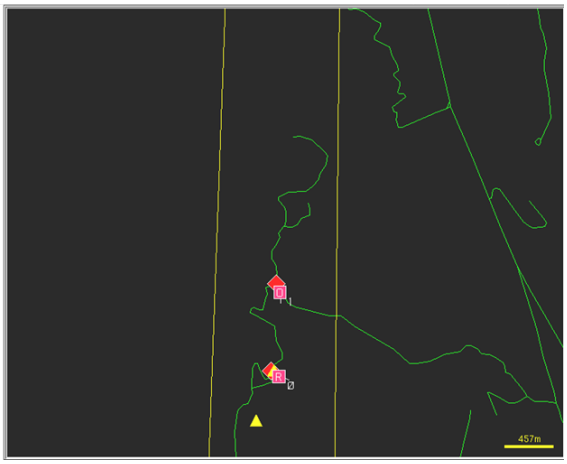

Figure 10a Detections, truth, and tracks for standard STAP processing for one CPI shown on ALPHATECH's MHT testbed display (DM++)

Figure 10b Detections and truth for KASTAP processing for one CPI shown on ALPHATECH's MHT testbed display (DM++).

Because past CPIs contain additional local training data, the covariance estimates calculated using the clutter map can improve the performance of standard STAP algorithms that employ range-averaged covariance matrices. A published technique for fusing calculated and conventional covariance estimates was used to produce a STAP weight vector that is robust to errors caused by effects such as internal clutter motion and antenna pattern mismatch.

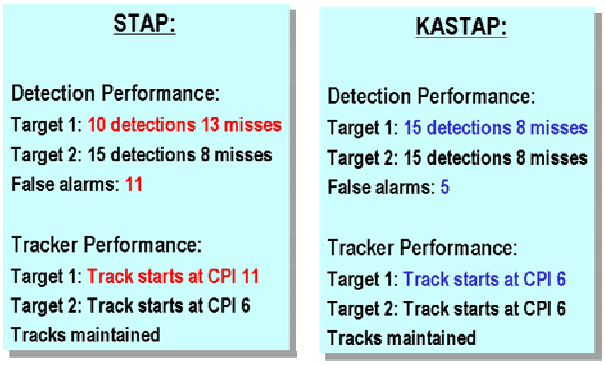

Figure 11 Tracker performance summary for standard STAP (left) vs. KASTAP (right) processing

The algorithm was applied to the KASSPER Data Set using a reduced degree of freedom, post-Doppler STAP framework. The effects of strong discretes and targets were suppressed from the covariance estimates in each Doppler filter. Performance was characterized in terms of SINR loss, target detections and false alarm locations, ROC curves, and track life. The results all show a significant benefit to employing knowledge aided STAP processing using past CPI reflectivity maps. Additional evaluations and refinements to produce further improvements in STAP performance are currently under investigation.

APPENDIX A

We give here the solution to Eqs. (2) for the position of a ground scatterer. We first define three orthonormal unit vectors as follows:

$$\hat{u}_v = \frac{\vec{V}_p}{|\vec{V}_p|}$$
$$\hat{u}_1 = \frac{\hat{u}_v \times \vec{r}_p}{|\hat{u}_v \times \vec{r}_p|} \qquad \text{(A.1)}$$
$$\hat{u}_2 = \hat{u}_v \times \hat{u}_1$$

Recall that $\vec{V}_p$ is the radar platform velocity vector and $\vec{r}_p$ is the position of the platform relative to the center of the earth. Next, we expand the scatterer position relative to the platform as

$$\vec{r}_{sc} - \vec{r}_p = R_s \cdot (a \cdot \hat{u}_v + b \cdot \hat{u}_1 + c \cdot \hat{u}_2) \qquad \text{(A.2)}$$

The first of Eqs. (2) becomes

$$\begin{aligned} &|\vec{r}_{sc}-\vec{r}_p|^2 = R_s{}^2\cdot(a^2+b^2+c^2) = R_s{}^2 \\ &\Rightarrow a^2+b^2+c^2 = 1 \end{aligned} \tag{A.3}$$

Next the expansion (A,2) is substituted into the second of Eqs. (2) to yield

$$\begin{aligned} &(\vec{r}_{sc}-\vec{r}_p)\bullet\vec{V}_p \\ &\quad = R_s\cdot(a\cdot\hat{u}_v + b\cdot\hat{u}_1 + c\cdot\hat{u}_2)\bullet(V_p\hat{u}_v) \\ &\quad = R_s\cdot V_p\cdot(a\cdot 1+0+0) = R_s\cdot V_p\cdot a \\ &\quad = R_s\cdot V_p\cdot\cos\theta_c \\ &\Rightarrow\ a = \cos\theta_c \end{aligned} \tag{A.4}$$

Substituting Eq. (A.4) into Eq. (A.3) yields

$$b^2+c^2 = 1-\cos^2\theta_c = \sin^2\theta_c \tag{A.5}$$

This allows us to define a polar angle β such that

$$\begin{aligned} b &= \sin\theta_c\cdot\cos\beta \\ c &= \sin\theta_c\cdot\sin\beta \end{aligned} \tag{A.6}$$

We next rewrite the magnitude squared of the scatterer position vector as follows

$$\begin{aligned} |\vec{r}_{sc}|^2 &= |\vec{r}_p+\vec{r}_{sc}-\vec{r}_p|^2 \\ &= |\vec{r}_p|^2 + 2\cdot\vec{r}_p\bullet(\vec{r}_{sc}-\vec{r}_p) + |\vec{r}_{sc}-\vec{r}_p|^2 \end{aligned} \tag{A.7}$$

Substituting the expansion (A.2) into Eq. (A.7) and using Eqs. (A.4) and (A.6) yields

$$\begin{aligned} |\vec{r}_{sc}|^2 = |\vec{r}_p|^2 &+ 2\cdot R_s\cdot\vec{r}_p\bullet(\cos\theta_c\cdot\hat{u}_v \\ &+ \sin\theta_c\cdot\cos\beta\cdot\hat{u}_1 \\ &+ \sin\theta_c\cdot\sin\beta\cdot\hat{u}_2) + R_s{}^2 \end{aligned} \tag{A.8}$$

We next use the fact that, from Eq. (A.1), $\vec{r}_p\bullet\hat{u}_1 = 0$ to give

$$\begin{aligned} |\vec{r}_{sc}|^2 = |\vec{r}_p|^2 &+ 2\cdot R_s\cdot(\cos\theta_c\cdot\vec{r}_p\bullet\hat{u}_v \\ &+ \sin\theta_c\cdot\sin\beta\cdot\vec{r}_p\bullet\hat{u}_2) + R_s{}^2 \end{aligned} \tag{A.9}$$

Substituting this result into the third of Eqs. (2) gives

$$\begin{aligned} (R_e+h)^2 = |\vec{r}_p|^2 &+ 2\cdot R_s\cdot(\cos\theta_c\cdot\vec{r}_p\bullet\hat{u}_v \\ &+ \sin\theta_c\cdot\sin\beta\cdot\vec{r}_p\bullet\hat{u}_2) + R_s{}^2\ , \end{aligned} \tag{A.10}$$

which can be solved for $\sin\beta$:

$$\sin\beta = \frac{(R_e+h)^2 - |\vec{r}_p|^2 - 2\cdot R_s\cdot\cos\theta_c\cdot\vec{r}_p\bullet\hat{u}_v - R_s{}^2}{2\cdot R_s\cdot\sin\theta_c\cdot\vec{r}_p\bullet\hat{u}_2} \tag{A.11}$$

There will generally be two different solutions for β giving the same value of $\sin\beta$:

$$\beta = \arcsin(\sin\beta),\quad \pi - \arcsin(\sin\beta) \tag{A.12}$$

The solution selected was the one that produced a scatterer position that was closest to the antenna pre-steering look direction. From Eqs. (A.2), (A.4), (A.6), and (A.12), the scatterer position vector is then finally given by

$$\begin{aligned} \vec{r}_{sc} = \vec{r}_p + R_s\cdot\{&\cos\theta_c\cdot\hat{u}_v \\ &+ \sin\theta_c\cdot(\cos\beta\cdot\hat{u}_1 + \sin\beta\cdot\hat{u}_2)\} \end{aligned}$$

APPENDIX B

We specify here the form of the steering vector to a ground scatterer with known position vector $\vec{r}_{sc}$. The steering vector is specified by spatial and temporal responses. The spatial response of a scatterer is defined by an N by 1 spatial steering vector (N is the number of antenna elements). Assuming the far-field approximation and identical antenna element patterns, the spatial steering vector elements are given by

$$[\vec{q}]_n = \exp(j\frac{2\pi}{\lambda}\vec{r}_n\bullet\hat{e}_{sc}),\quad n = 1,2,...N \tag{B.1}$$

Here, $\vec{r}_n$ is the position vector to the nth antenna element and $\hat{e}_{sc}$ a unit vector from the platform to the ground scatterer. This unit vector is given in terms of the azimuth and elevation angles of the scatterer

$$\hat{e}_{sc} = \cos(el)\cdot\sin(az)\cdot\hat{e}_{East} + \cos(el)\cdot\cos(az)\cdot\hat{e}_{North} + \sin(el)\cdot\hat{e}_{Up} \quad \text{(B.2)}$$

Here, $\hat{e}_{East}, \hat{e}_{North}, \hat{e}_{Up}$ are unit vectors pointing east, north, and up respectively at the location of the radar platform. The azimuth angles were determined by converting the scatterer position relative to the platform $(\vec{r}_{sc} - \vec{r}_p)$ from earth-centered to platform-centered east-north-up coordinates. Due to atmospheric refraction, however, the elevation angles computed in this manner do not accurately give the actual elevation angle of the radar return. Thus, the elevation angles were re-computed for an effective earth model using the following equation:

$$\sin(el) = \frac{\{2\cdot kR_e\cdot(h-h_p) + h^2 - {h_p}^2 - {R_s}^2\}}{2\cdot R_s\cdot(kR_e + h_p)} \quad \text{(B.3)}$$

Here, h_p is the height of the radar platform above the spherical earth, and $kR_e = (4/3)\cdot R_e$ is the effective earth radius, which accounts for atmospheric refraction near the earth's surface.

Letting M be the number of pulses, the temporal response of a scatterer will be represented by an M by 1 column vector. The temporal steering vector elements will be given by

$$[\vec{t}]_m = \exp[j\cdot 2\pi\cdot f_{Dop}T\cdot(m-1)], \quad m = 1,2,...M \quad \text{(B.4)}$$

where f_{dop} is the Doppler frequency of the scatterer, T is the pulse repetition interval, and m the pulse index within the CPI.

The total space-time steering vector to a given scatterer will be a NM by 1 column vector which is the direct product of the spatial and temporal steering vectors. The elements of the steering vector are then written as

$$[\vec{s}]_{nm} = [\vec{q}]_n\cdot[\vec{t}]_m,$$

or more succinctly,

$$\vec{s} = \vec{q}\otimes\vec{t} \quad \text{(B.5)}$$

This form was used for the steering vectors $\vec{s}_i$ to each ground scatterer appearing in Eqs. (3)-(6) and Eq. (9).

ACKNOWLEDGMENT

The authors would like to thank DARPA for funding this work under contract F30602-02-C-0010.

REFERENCES

[1] William L. Melvin, "Space-Time Adaptive Radar Performance in Heterogeneous Clutter" *IEEE Trans. Aerospace Elec. Sys.*, Vol. 36 No. 2, pp. 621-633 (April, 2000).

[2] William L. Melvin, Joseph R. Guerci, Michael J. Callahan, Michael C. Wicks, "Design of Adaptive Detection Algorithms for Adaptive Surveillance Radar", IEEE International Radar Conference, Arlington, VA, May 2000

[3] "High-Fidelity Site-Specific Radar Simulation: KASSPER Data Set 2", Information Systems Laboratories, Inc. October, 2002

[4] J. Bergin, J. Guerci, P. Techau, C. Teixeira, "Space-Time Beamforming with Knowledge-Aided Constraints", Adaptive Sensor Array Processing Workshop 2003, 11-13 March 2003

[5] R.C. DiPietro, "Extended Factored Space-Time processing for Airborne Radar", Proc. 26th ASILOMAR Conf., Pacific Grove, CA, pp. 425-430 (October 1992)

[6] J. R. Guerci, "Theory and Application of Covariance Matrix Tapers for Robust Adaptive Beamforming", *IEEE. Trans. Signal Processing*, Vol. 47, No. 4, pp. 977-985 (April 1999)

[7] F. C. Robey, D. R. Fuhrmann, E. J. Kelly, and R. Nitzberg, "A CFAR adaptive matched filter detector", *IEEE Trans. Aerospace Elec. Sys.,* vol. 28 no. 1, pp. 208-216, (January 1992)